ANALYSIS OF BASE-HEATING ENVIRONMENT DURING GROUND TESTING OF A LUNAR LANDER DEMONSTRATOR

T. S. Wang, F. Canabal, K. S. Knox, and R. F. Hawkins
NASA Marshall Space Flight Center
Huntsville, AL

M. Bergman
Masten Space Systems
Mojave, CA

ABSTRACT

A three-dimensional, unstructured-grid, pressure-based, reacting flow, computational fluid dynamics and heat transfer methodology was employed to study the base-heating environment of a lunar lander demonstrator, during terrestrial ground testing. Two base-heating environments were investigated: lunar lander demonstrator sitting on pad, and lunar lander demonstrator hovering at a distance above ground. Two unique and quite different base-flow physics are found for these two cases. In the case of demonstrator sitting on pad, the computed heat fluxes are high and the base flow is unsteady, caused by a Coanda effect precursor that makes the fountain jet oscillate about the center of the base. For the second case, due to the higher elevation of the demonstrator and the layout of the nozzles, the Coanda effect forces the fountain jet to be attached to two of the nozzle plumes, resulting in much lower computed base heat fluxes.

NOMENCLATURE

Q   = heat flux

T   = temperature

X,Y,Z   = coordinates

SUBSCRIPTS

c   = convective

o   = reference property for non-dimensionalization

r   = radiative

INTRODUCTION

The lunar lander demonstrator, known as XL-1T (terrestrial), is a collaborative effort between Masten Space Systems and NASA, under NASA's Lunar CATALYST (also known as Lunar Cargo Transportation and Landing by Soft Touchdown) initiative. The lunar lander demonstrator is a reusable Vertical-Takeoff, Vertical-Landing (VTVL) terrestrial test-bed, for Masten's powered-descent landing system. It is controlled by four throttleable main engines utilizing green hypergolic propellants. Masten's approach to XL-1T is to create an affordable terrestrial test-bed to feed the design of their lunar vehicle, XL-1. To test the XL-1T terrestrially,

one of the concerns for a four-engine vehicle such as the lunar lander demonstrator, is the potential of a severe base-heating environment, caused by the formation of a "fountain jet" during testing. Fountain jet is a unique base flow physics which was discovered during the development of the Delta Clipper Experimental (DC-X) vehicle.

The DC-X was the prototype of a reusable single-stage-to-orbit launch VTVL vehicle built by McDonnell Douglas, in cooperation with NASA from 1994 to 1996. The four-engine DC-X was developed to demonstrate a totally reusable vehicle. The descent portion of the trajectory requires unique flight maneuvers such as a retrothrust maneuver for deceleration and a powered vertical landing. These flight maneuvers of the DC-X induce a severe base-heating environment due to the formation of the fountain jet. Under a Cooperative Agreement between McDonnell Douglas/Boeing and Marshall Space Flight Center, a structured-grid, pressured-based, coupled computational fluid dynamics (CFD) and radiative transport equation solver – FDNS[1], was used to analyze a complicated base-flow field and predict the base-heating environment for the DC-X during its on-ground operation[2].

The computational study found that the four-engine clustered nozzle plume-to-ground impingement produces two kinds of ground-jets: an outward going ground-jet that rushes toward the ambient atmosphere, and an inward going ground-jet that converges under the vehicle and emerges as a fountain-jet. The direct impingement of the fountain-jet with the vehicle base is the source for the high convective base-heating loads. Following the impingement, the fountain jet transformed into a wall jet that flows across base surface. At the same time, the pumping action of the nozzle exhaust plume and fountain jet entrains air that turbulently mixes with any existing unburnt fuel, enabling plume afterburning, which adds to the convective heating. Simultaneously, radiator like steam that is present in the high temperature plume and fountain-jet, contributes to base radiative heating also. Finally, the outward-going base wall jet and ground-jet, along with the entrained air, roll up to form large vortices that is the exhaust-plume growth.

The fountain jet is hotter and stronger than the reverse jet formed during flight at altitude, because the nozzle plumes near ground have not expanded and diluted, and the after-burning reactions are at their highest at sea level. In that study[2], the plume after-burning was computed with finite-rate chemistry. The FDNS predicted peak base convective and radiative heat fluxes with finite-rate chemistry that compared very well with those of test data. Without the finite-rate chemistry, the predicted peak base convective and radiative heat fluxes dropped significantly from those computed with the finite-rate chemistry, signifying the importance of plume afterburning during ground testing. Also, it was discovered that DC-X generates a stable fountain jet, possibly due to the entire vehicle was covered by an aeroshell, resulting in a smooth and flat base. And the distance between the nozzles is large, resulting in minimal interaction between the fountain jet and four nozzle plumes.

In terms of base-flow physics, it is anticipated that there will be a lot of similarities between those of DC-X and the lunar lander demonstrator, since both VTVL vehicles have a four-engine clustered nozzle configuration. However, it was also speculated that there may be subtle differences between the two vehicles due to the differences in geometry, nozzle layout, and propellants utilized. Historically, a series of catastrophic launch vehicle failures[3] have been reported, due to a lack of understanding of the base flow physics. Accurate prediction of the base heat fluxes and understanding of the base flow physics for various design conditions are therefore vital to the success of any new vehicle development. In this effort, two cases were studied using an anchored computational methodology. The first case is the theoretical worst case where the lunar lander demonstrator is sitting on pad. The second case assumes the demonstrator hovering at a distance above ground.

COMPUTATIONAL METHODOLOGY

COMPUTATIONAL FLUID DYNAMICS AND HEAT TRANSFER

The computational fluid dynamics (CFD) and heat transfer code UNIC[4-5] used in this study, is based on a multi-dimensional, finite-volume, viscous, chemically reacting, unstructured-grid, and pressure based formulation. UNIC code was developed based on its structured-grid predecessor - the FDNS code[1]. Time-varying transport equations of continuity, species continuity, momentum, total enthalpy, turbulent kinetic energy, and turbulent kinetic energy dissipation were solved using a time-marching sub-iteration scheme.
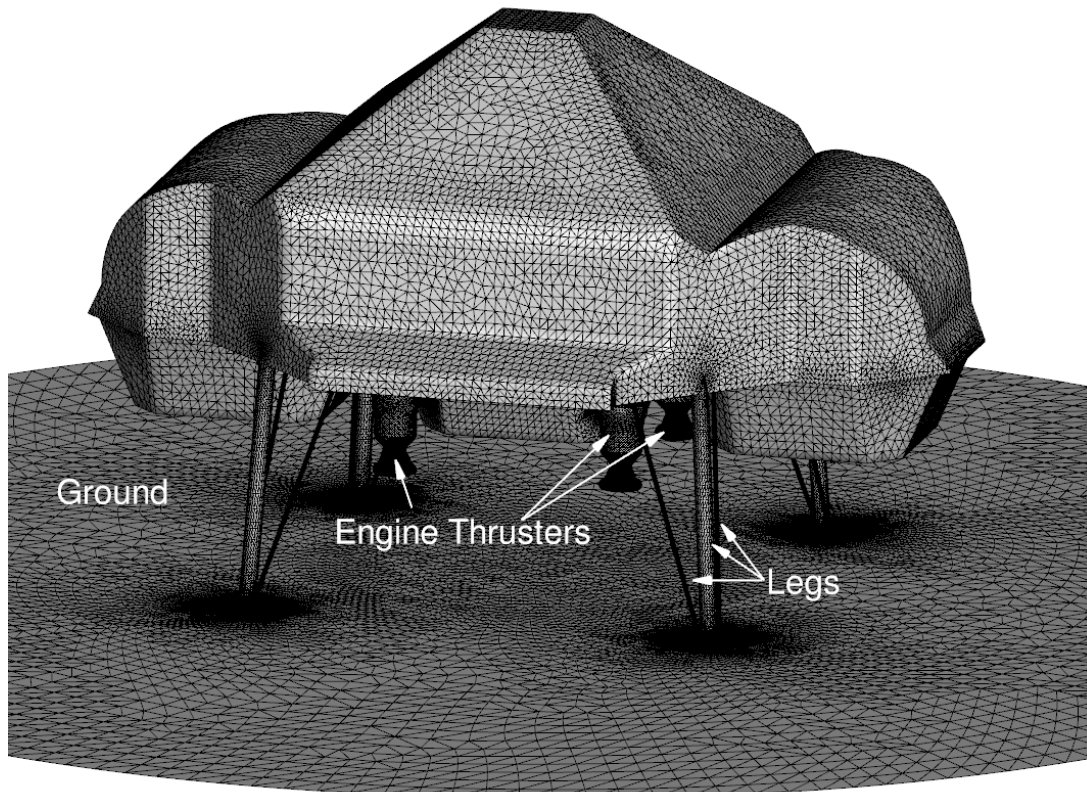

Figure 1. Face meshes of Grid 1 for the lunar lander demonstrator sitting on pad.

A predictor and corrector solution algorithm was employed to provide coupling of the governing equations. A second-order central-difference scheme was employed to discretize the diffusion fluxes and source terms. For the convective terms, a second-order upwind total variation diminishing difference scheme was used. If the temporal accuracy is required, a second-order backward difference scheme can be employed to discretize the temporal terms. Point-implicit method was used to solve the chemical species source terms. Sub-iterations within a time step were used for driving the system of second-order time-accurate equations to convergence. Details of the numerical algorithm can be found in references[6-11].

An extended k-ε turbulence model[12] was used to describe the turbulence. A modified wall function approach was employed to provide wall boundary layer solutions that are less sensitive to the near-wall grid spacing. Consequently, the model has combined the advantages of both the
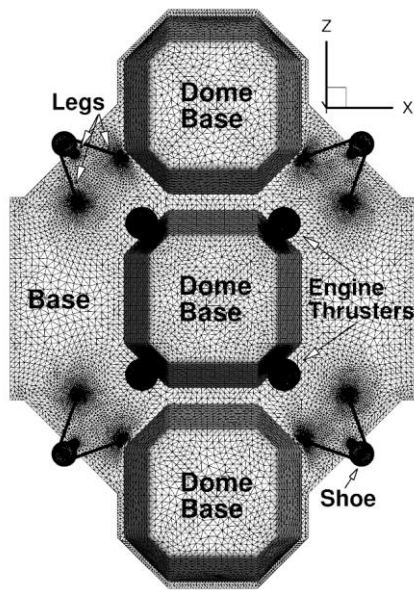
Figure 2. Face meshes for the lunar lander demonstrator base.

integrated-to-the-wall approach and the conventional law-of-the-wall approach by incorporating a complete velocity profile and a universal temperature profile[11].

In addition, combustion products like H_2O and CO_2 are radiators that contribute to the base heat fluxes. The radiative field is analyzed by solving the radiative transport equation[13-14]. The discrete ordinate method was used to solve the radiative transport equation. A weighted-sum-of-gray-gases model was used to calculate the emissivity and absorptivity of the radiation medium[15].

The base-flow heating physics pertinent to this study were anchored or studied in earlier efforts with both FDNS and UNIC codes. For example, a base-pressure characteristic curve was benchmarked for a four-engine cluster nozzle[16], the base drag of flow over DC-X at altitudes[17] and base heat fluxes of an in-ground Delta Clipper-Experimental[2] were anchored. In addition, the prediction of base-heating environment for X-33[18] and investigation of the effects of base-bleed[11] and fence[19] on the base heat fluxes were also performed. The anchoring of base radiative heat fluxes with a single aerospike engine test and prediction of base heating environment during three potential power-pack out scenarios were also conducted[11].

GASRAD PLUME RADIATION ENGINEERING MODEL

Plume radiation using GASRAD code[20-21] is calculated in a two-step process. First the nozzle plume flowfield is computed, and then the GASRAD is applied. GASRAD uses line-of-sight method integrated over a hemisphere to calculate radiative heat flux on vehicle body points receiving radiation from exhaust plumes and uses a narrow-band model for radiation properties[22]. The regular plume flowfield generator, however, does not take into account plume-to-plume or plume-to-surface interactions. In addition, the complicated base-flow physics such as fountain jet-to-base or plume-to-ground impingement cannot be easily modeled using such an engineering method. In order to account for those physics, two axisymmetric slices were extracted from the UNIC solution; one for the fountain jet, another for the plume-to-ground interaction. These slices are then rotated and added into the nozzle plumes for the radiation calculations.
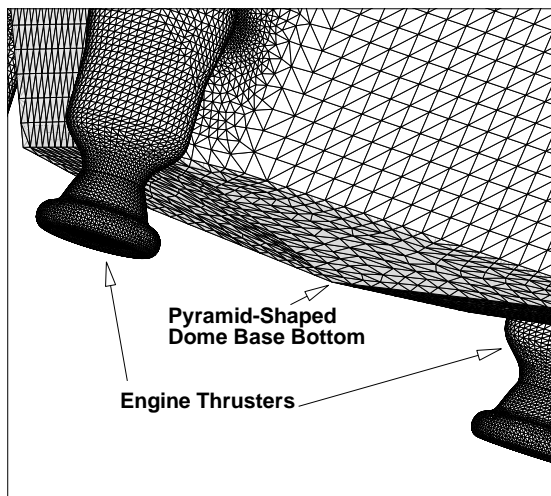

Figure 3. Face meshes for the central dome base and the thrusters.

COMPUTATIONAL GRID GENERATION

Computational grid generation started with a computer-aided design file, which contains the surface geometry of major components of the lunar lander demonstrator. A surface generator was used to simplify and stitch the raw surfaces in order to form a water-tight domain comprised of multiple faces. This surface generator was then used to generate surface meshes on the multiple faces. Finally, a volume mesh generator was used to generate volume cells for computational fluid dynamics computations. In total, three computational meshes were generated.

Figure 1 shows the computational face meshes of Grid 1, depicting the lunar lander demonstrator sitting on pad, or ground. The non-dimensional base-to-ground distance for this nominal case is unity. This lunar lander demonstrator uses four engines to propel the vehicle, along with four leg assemblies to support the weight of the vehicle while resting on the ground. Each leg assembly contains one large-diameter compression member and two smaller-diameter tension members.

Figure 2 shows the face meshes for the lunar lander demonstrator base, viewing from the ground, or y-direction. The vehicle base is comprised of a flat base and three dome bases that protrude from the flat base. All three dome bases are identical in dimensions. Figure 2 also shows the layout of the components such as the legs and the engine thrusters, relative to the flat base and the dome bases. It can be seen from this figure that this demonstrator is not geometrically symmetric to the base center. It is longer in the z-direction that comprises of three base domes, and shorter in the x-direction that has only one dome base.

Figure 3 shows a close-up look at the face meshes for the central dome base and the thrusters in sight. It can be seen that the dome base has a pyramid shaped bottom. The pyramid shape design provides more structural rigidity and ease of manufacturability. This pyramid shaped bottom contains four faces. It can be imagined that each face is partially shielded by the opposite face from radiative heating. The central dome base is closely surrounded by the four engine thrusters. Intuitively, the tip of the central dome base is subject to the highest base heating since not only is it located at the geometrical center of
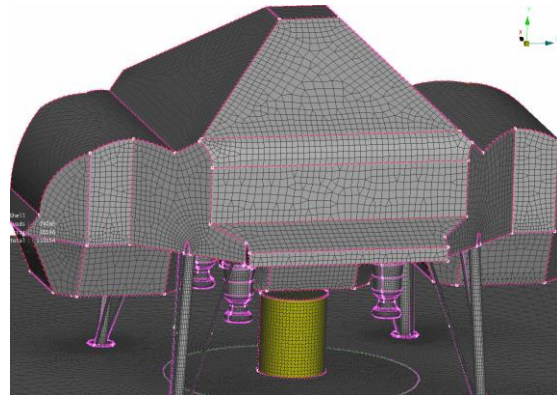

Figure 4. Initial face meshes with one source cylinder for Grid 2.
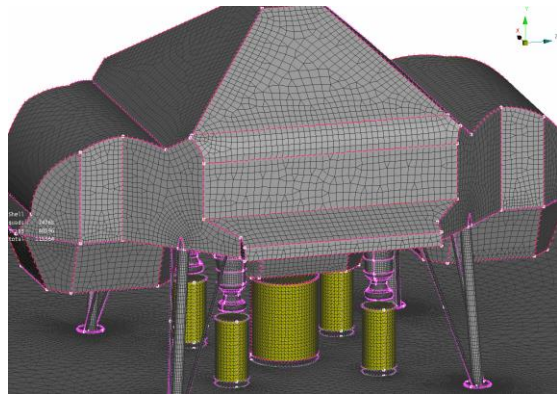

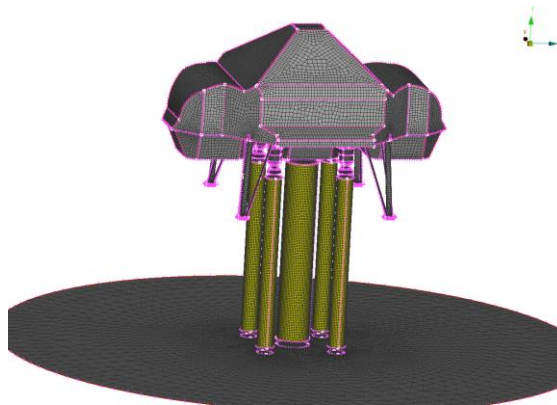Figure 5. Initial face meshes with five source cylinders for Grid 3.

Figure 6. Initial face meshes with five source cylinders for Grid 4.

the base, it is also the closest point to the ground. If a line is to connect the three tips of the dome bases, the pair of thrusters on either side of that line are canted outward 3 degrees. That means the nozzle plumes are not perpendicular to the ground, but canted 3 degrees, making the inward ground jet less than that of thrusters perpendicular to the ground.

The volume grid generator uses advancing-front locally-reconnect (AFLR) method to create mostly tetrahedral cells from the boundary layer of solid surfaces. Comparing to the transfinite interpolation method, AFLR method is an efficient way of generating volume cells for complicated vehicle geometry like the lunar lander demonstrator. On the other hand, this method can control the cell size distribution very well for the wall boundary layer, but the action region such as the nozzle plumes and fountain jet require inserting additional faces called source cylinders.
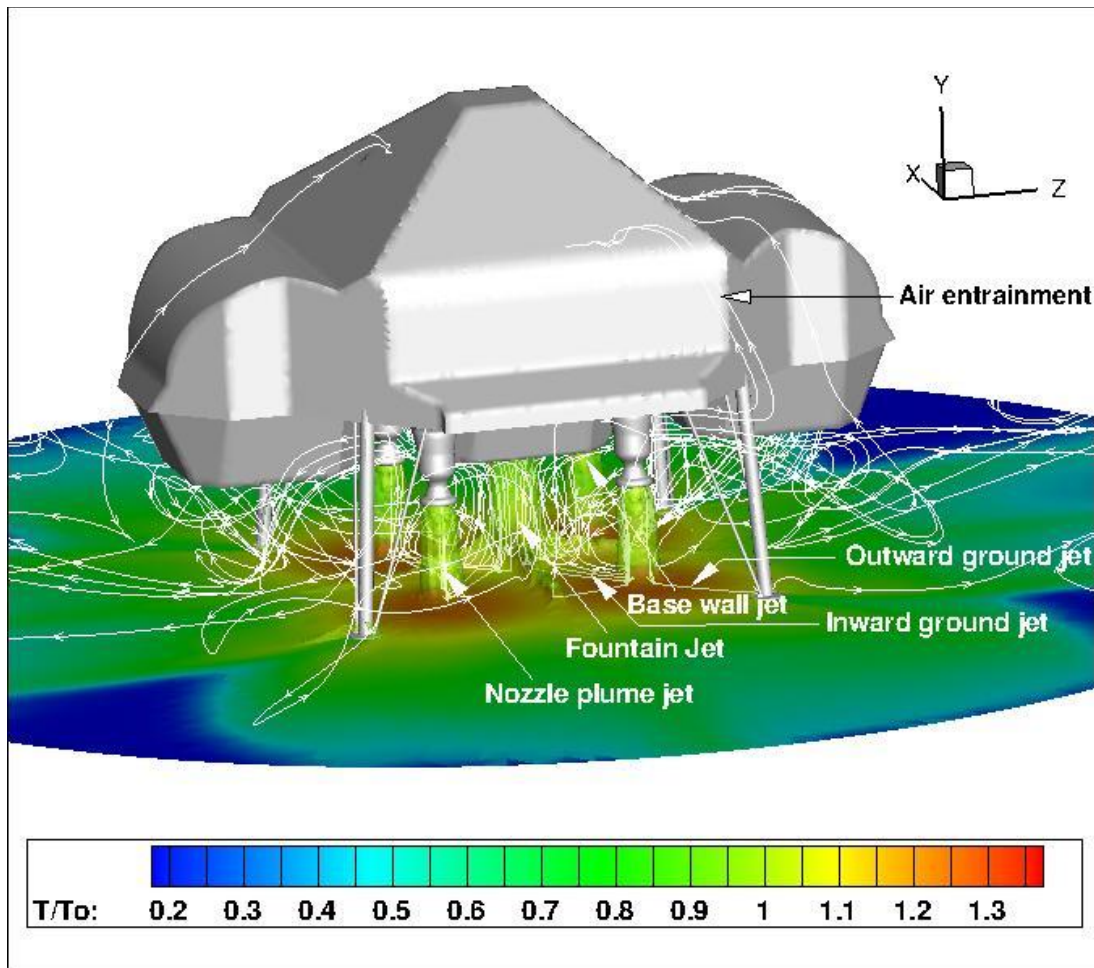

Figure 7. Computed base-flow physics for lunar lander tested on pad.

Source cylinders are hollow cylinders that user can generate to cover a particular flow region of interest, e.g., the fountain jet. By assigning desired cell sizes on that cylinder, the advancing-front locally-reconnect method fills the inside of that source cylinder with cell sizes related to the cell size assigned on the faces of the source cylinder, therefore controlling and improving the grid resolution of the fountain jet.

Figure 4 shows the initial face meshes with one source cylinder for Grid 2. It can be seen that the source cylinder of Grid 2 goes from near ground to near the bottom of the central dome base, therefore covering the fountain jet region. Figure 5 shows the initial face meshes with five

source cylinders for Grid 3. It can be seen that not only the fountain jet is covered, the four nozzle plumes are also covered, thereby enhancing not only the grid resolution of the fountain jet, but also that of the four nozzle plumes. The total number of cells of Grid 1, Grid 2, and Grid3 are 12,979,470, 15,926,621, and 13,843,266 cells, respectively. The computational results of these three grids served the purpose of a grid study.

Figure 6 shows the initial face meshes with five source cylinders for Grid 4, for computing the base flow environment when the base-to-ground distance is raised 4.3 times from that of the nominal case. Grid 4 follows the steps of Grid 3, except the height of the demonstrator is increased. For consistency in grid density for source cylinders between Grid 3 and Grid 4, the grid density of the source cylinders in Grid 4 is identical to that of Grid 3. The total cell number of Grid 4 is increased to 16,983,366 cells.
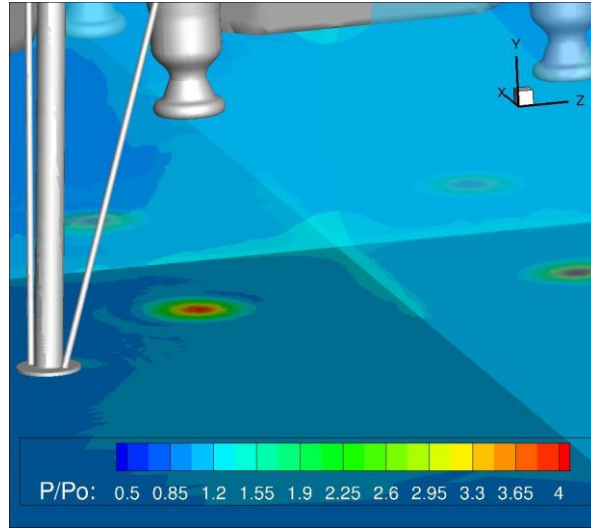

Figure 8. Computed pressure contours.

RESULTS AND DISCUSSION

The four throttleable main engines of the Masten's powered decent landing system utilizes green hypergolic propellants containing sodium (Na) and boron (B). Equilibrium calculation of those propellants resulted in seventeen species. To improve the computational efficiency, three trace species were eliminated and fourteen species were considered for computational fluid dynamics computations. These fourteen species are H_2O, O_2, H_2, O, H, OH, CO, CO_2, HBO_2, $NaBO_2$, Na, NaOH, BO_2, and N_2. To reduce the total number of computational cells in a three-dimensional domain, an axisymmetric thruster computation was conducted first. The resulting flow properties at the axisymmetric nozzle exit plane were then mapped to the thruster nozzle exit planes of the three-dimensional computational grid for the actual computations. Fixed flow property boundary condition was used at the nozzle exit plane. Non-slip wall boundary condition was applied to all solid surfaces. A floating property boundary condition was utilized for the freestreams, where one atmosphere pressure was used for the ambient. Initial total conditions were applied when the flow is reversed at the freestream boundary. It is noted that since the finite-rate afterburning kinetics mechanisms are not readily available for exotic species involving sodium and boron, equilibrium chemistry option was activated in lieu of that of finite-rate chemistry.
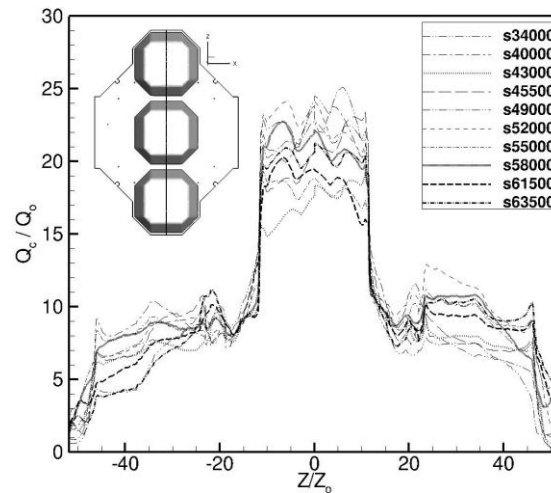

Figure 9. Computed base convective heat fluxes along a wetted distance in z-direction.

ENVIRONMENT FOR LUNAR LANDER DEMONSTRATOR FIRING ON PAD

When the lunar lander demonstrator is tested on pad, the distance between center of base dome and the ground is minimal, hence it is the worst scenario in terms of base heating. Figure 7 shows the computed base-flow physics using temperature contours and iso-temperature, along with streamlines. An iso-temperature is picked such that the fountain jet and four nozzle plumes can best be represented, as shown in Fig. 7. It can be seen that the four nozzle plumes impinge on the ground, leaving hot temperature imprints (from temperature contours on ground), and forming ground jet. As described in the computational grid generation section, due to the layout of the canted thrusters, which are not symmetric to the geometrical center of the base, but symmetric to the xy- and yz-planes, the inward flowing ground jet from the four plumes meet along the symmetric planes and forming two ridges on the ground. A fountain jet can be seen emerging from the intersection of the two ridges and rises all the way to impinge upon the center of the central dome base. This impingement forms a wall jet that flows over the structures of the base region that eventually exhausts into the atmosphere. The streamlines help the visualization of the nozzle plume jet,

Figure 10. Computed base convective heat fluxes along a wetted distance in x-direction.

inward and outward ground jet, fountain jet, along with base wall jet. It can be seen that part of the plumes or outward going ground jet will go up the demonstrator body followed by entrained air. The most important air entrainment happens along the free shear layers of the hot nozzle plumes and fountain jet, where any unburnt propellant in the mixing layers combines with oxygen in air and then afterburns, raising the temperature in the mixing layers.
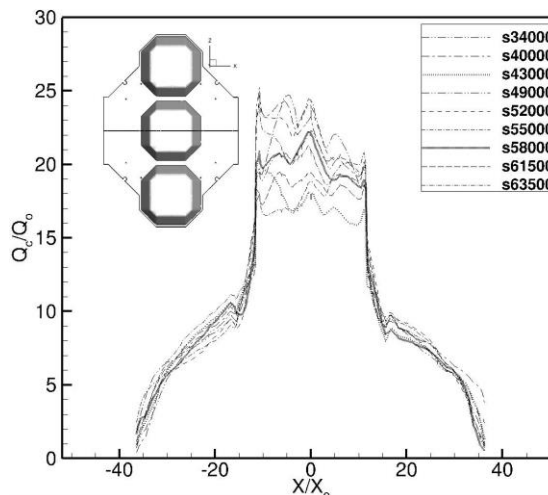
Figure 8 shows the computed pressure contours on the ground and two symmetry planes that pass through the geometrical centerline of the computational domain. Again, the four high pressure imprints due to the plume-to-ground impingement can be seen on the ground. In addition, near the bottom of the two symmetry planes, two ridges emerge from the ground. Obviously, these two ridges are formed at the foot of the symmetry planes where the inward ground jet meet. The pressure is higher at the intersection of the two ridges, coinciding with the formation of a fountain jet that can best be seen with the iso-temperature plot shown in Fig. 7.

Afterburning reactions make the nozzle plumes, and more importantly the fountain jet, hotter which proceeds to torch the base in the form of convective and radiative heating. The afterburning reactions also make the mixing layers of the nozzle plumes and fountain jet unsteady, creating pressure differences or oscillations. Compared to the four nozzle plume jets, the fountain jet is weaker, hence it becomes unsteady and starts to oscillate about the central dome base. This phenomenon can be related to the Coanda effect.

The Coanda effect is the tendency of a fluid jet to be attracted to an adjacent flat or curved surface[23]. The degree of attraction depends on the strength of the fluid jet and closeness of the fluid jet to the surface. The mechanism of the Coanda effect is explained as the following: When a fluid jet is adjacent to a surface, the fluid jet entrains fluid from the surroundings such that a region of lower pressure develops between the fluid jet and the surface. This low pressure

region forces the fluid jet to move closer to the surface. Often when the fluid jet is close enough to the surface, the fluid jet attaches to the surface.
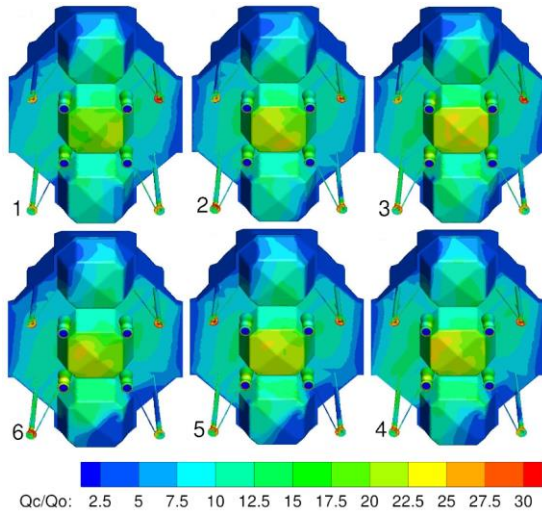

Figure 11. Computed base convective heat flux contours over elapsed times.

In the case of lunar lander demonstrator firing on pad, the fountain jet is a weaker jet compared to the strength of its parental nozzle plumes. Some low pressure regions develop between the nozzle plumes and the fountain jet, and the fountain jet becomes attracted to the surface of the plumes. Note the surface of the parent plumes is not a solid surface hence the surface of the parent plumes is likewise unsteady. In addition, while firing on pad, the weaker fountain jet is weak enough to be attracted to the lowest pressure region among itself and the four nozzle plumes, yet remains strong enough to return quickly to the center while searching for another low pressure region. As a result, the fountain jet is oscillating randomly among the nozzle plumes but never attached to any one of the nozzle plumes, resulting in an asymmetric, unsteady heat flux contours on the base domes as time elapses. Since the fountain jet never attaches to any of the nozzle plumes, to differentiate this special phenomenon from the true Coanda effect and for lack of a better terms, it is described as a Coanda effect precursor herein.

Figure 9 shows a series of computed base convective heat flux profiles along the wetted distance in z-direction at various number of iteration steps. This is created by plotting the surface convective heat fluxes along the intersection of yz-plane with the base components. It can be seen from the insert that this wetted line passes though the center line of the base domes. It can also be seen that the higher convective heat fluxes occur on the central base dome, which is reasonable since the fountain jet is oscillating about the central base dome, but never attached to any one of the nozzle plumes. The varying level of the convective heat fluxes at various iteration steps show the unsteady nature of the fountain jet, primarily due to the Coanda effect precursor phenomenon. Figure 10 shows a series of computed base convective heat flux profiles along the wetted distance in x-direction, which are obtained by plotting the surface convective heat fluxes along the intersection of the xy-plane with the center of the central dome base. In the x-direction, the wetted distance only passes through the central dome base. Once again, it can be seen the effect of the unsteady fountain jet on the central dome base, where the computed base convective is oscillating with respect to the number of iterations, or the elapsed times.
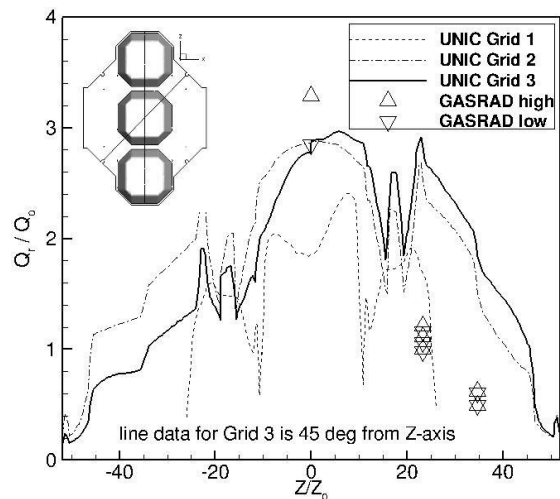

Figure 12. Comparison of computed radiative heat fluxes.

Figure 11 shows computed convective heat flux contours for the entire base components over elapsed times. These contours show not only the unsteady nature, but also the asymmetric shape of the fountain jet. It should be noted that other factors that could contribute to the asymmetric and unsteady flow features of this base flow environment include: flow over uncovered components such as base domes, thrusters, and legs; afterburning reactions in mixing layers of nozzle plumes and fountain jet; volume grid generator produced predominately tetrahedral cells, resulting in asymmetry in the volume grid; and the layout of the thrusters not being symmetric to the base center. In addition, the thrusters were canted three degrees outward in the +x and –x directions; and finally, the CAD file itself was not perfectly symmetric.
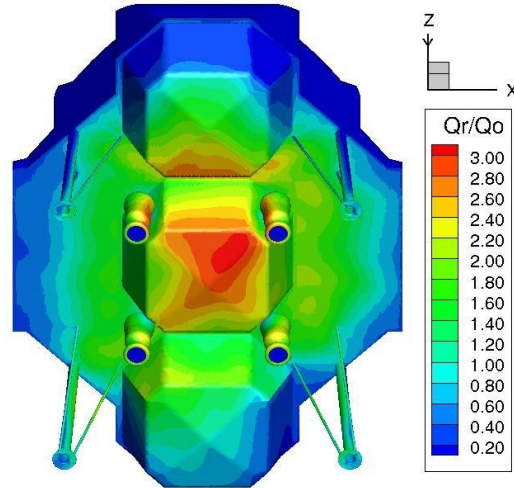

Figure 13. Computed radiative heat flux contours.

Figure 12 shows a comparison of the computed radiative heat fluxes along the wetted distance in z-direction, while those along the wetted distance in x-direction are shown in Figure 13. Results for Grid 3 are plotted along a slice that is 45 degrees from the z-axis, because the peak heat fluxes happened along that line, exhibiting the asymmetric nature of the fountain jet. It can be seen that without the source cylinders, the computed radiative heat fluxes for Grid 1 are too low. The computed radiative heat fluxes for Grid 2 and Grid 3, are similar, especially the peak fluxes. Additionally, the peak radiative heat fluxes for Grid 2 and Grid 3 are also bracketed by the high and low values calculated by engineering model GASRAD, and their values are closer to the low value. These two GASRAD values were obtained from a body point located at the central tip of the bottom section of the central dome base.

It should be noted that the GASARD result used a UNIC solution from Grid 3 to construct the fountain jet for its radiation calculation. In that UNIC solution, the fountain jet swayed to the upper-right corner of the central dome base, or 45 degrees from the z-axis, as shown in Figure 13. Hence, approximately a quarter of the fountain jet region was hot, while the other three-quarters of that region was colder. The high value GASRAD solution was obtained by taking a slice of the hot side of the fountain jet and rotating it to construct a whole fountain jet, whereas the low value GASRAD solution was acquired by using a slice of the colder side of the fountain jet. This could explain why the low value GASRAD solution agrees better with the UNIC computed peak radiative heat fluxes from Grid 2 and Grid 3.
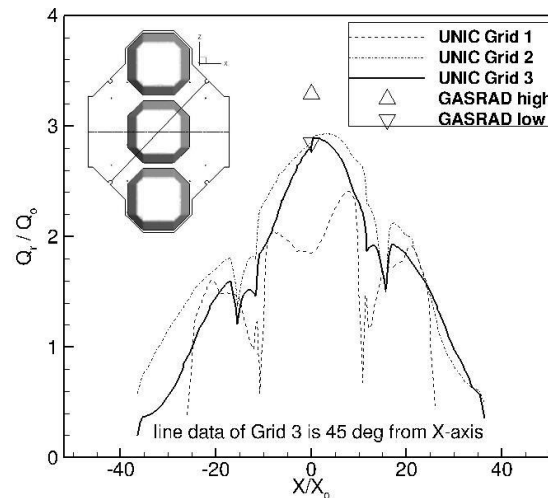

Figure 14. Comparison of computed radiative heat fluxes.

The radiative heat flux profiles in Figure 13 also show another two groups of GASRAD calculated radiative heat fluxes that are much lower than those from UNIC solutions on Grid 2 and Grid 3. This is due to the body point of one group (Z/Zo ~ 23) being located at a nearest corner of the bottom section of another dome base at the +z direction, while the body point of another group (Z/Zo ~ 35) is located at the central tip of that same dome base. Remember that the flowfield constructed for GASRAD is symmetric, but the radiative heat flux profiles of Grid 2 and Grid 3 apparently show the dome base located at the +z direction receives much higher radiation than that of the dome base in the opposite direction, as shown in Figure 13. This discrepancy is caused by the asymmetric nature of the fountain jet. Figure 14 shows a comparison of the computed radiative heat fluxes along the wetted distance in x-direction, which covers only the central dome base. The result is similar to that discussed in Figure 12, where the
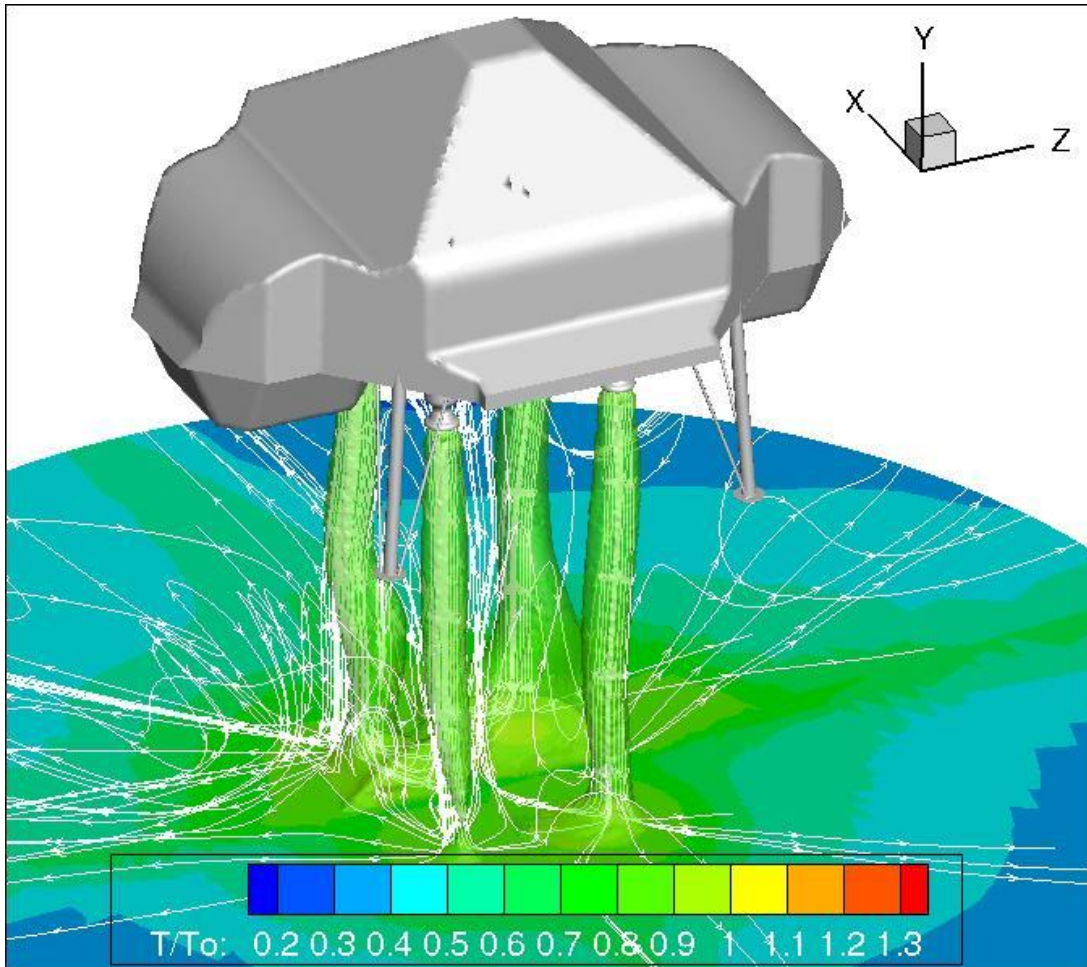

Figure 15. Computed base-flow physics for lunar lander hovering over ground.

computed radiative heat fluxes are too low from Grid 1, and both the computed peak heat fluxes from Grid 2 and Grid 3 are very close and bracketed by the high and low values from GASRAD engineering method.

ENVIRONMENT FOR LUNAR LANDER DEMONSTRATOR HOVERING OVER GOUND

Figure 15 shows the computed base-flow physics for the lunar lander demonstrator hovering over ground, using a selected iso-temperature to represent the fountain jet and the

nozzle plumes. It can be seen that due to the Coanda effect, the fountain jet is attached to the two nozzle plumes in the +x direction. This is very different from that occurred when the demonstrator is tested on pad.

When the lunar lander demonstrator is hovering over the ground, the distance from base center to the ground is about four times higher than that of lunar lander demonstrator firing on pad. With a chamber pressure lower than that of DC-X, and therefore a low mass flow rate, the elongated plumes are less stable over time. Also, the four nozzle plumes can expand more than those of firing on pad due to the longer traveling distance. In addition, these thrusters are canted outward and not perpendicular to the ground, which further weakens the plumes by the time they reach the ground, resulting in a weaker fountain jet than that of firing on pad, since there are more outward going ground jet than the inward going ground jet. Furthermore, the distances between the thrusters for lunar lander demonstrator are smaller than those of the DC-X, meaning the distance among the fountain jet and the nozzle plumes are shorter for the lunar lander demonstrator. Combining all of these factors just described above, the base flow environment of a hovering lander demonstrator provides a perfect opportunity for Coanda effect to take over.

It should be noted that the Coanda effect occurs over a short period of time and not immediately, as described in the elapsed time history of base convective heat flux contours shown in Figure 16. In the beginning, as shown in frame 1, the fountain jet was straight and not
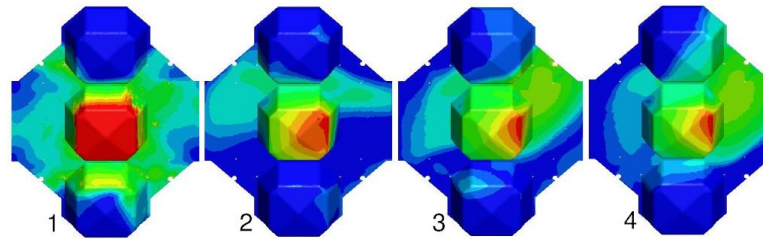

Figure 16. Computed convective heat flux contours at different elapsed times.

attaching to any of the nozzle plumes, and the peak convective heat flux is computed at 7.0. In time, the fountain jet is swaying to the +x direction and attached to the two plumes in the +x direction and the hot spot on the central base dome moves toward the +x direction, or right-hand-side of the central dome base, as shown in frame 2, and the peak convective heat flux drops to 5.3. As time increases, the hot spot keeps on moving to the right-hand-side of the central dome base, and peak heat flux drops to 4.1 in frame 3. Eventually, the peak convective heat flux settles at around 5.3 in frame 4. The computational result shows that once attached, the fountain jet stays attached and is never able to come back to the center of the base dome.

It can be speculated that if the hovering height is raised further, there will be a point where the fountain jet disappears. At which time, the effect of fountain jet on base heating diminishes.

Table 1. A comparison of computed peak base heat fluxes

	Base-to-ground Y/Y_o	Grid	Q_c / Q_o	Q_r / Q_o
UNIC non-reacting flow	1	1	16.5	-
	1	2	17.2	-
	1	3	16.7	-
UNIC reacting flow	1	1	20.0	2.4
	1	2	22.6	2.9
	1	3	22.7	3.1
GASRAD	1	3	-	2.85~3.29
UNIC reacting flow	4.3	4	5.3	0.9

Table 1 shows a comparison of computed peak base heat fluxes for both cases. For lunar lander demonstrator tested on pad, the computed peak base heat fluxes with the reacting

flow option are on average 30% higher than those with the non-reacting flow option, indicating the importance of plume afterburning physics during the demonstrator on pad testing. This also agrees with the observation from the Delta Clipper-Experimental in-ground effect study[2]. In UNIC reacting flow results, the computed peak convective and radiative heat fluxes for Grid 2 and Grid 3 are very close and are higher than those of Grid 1, showing the importance in resolving the physics of fountain jet and nozzle plumes, especially in the fountain jet region. The agreement between the results of Grid 2 and Grid 3 indicates the solutions of both grids have reached approximate grid independence. For peak radiative base heat fluxes, the GADRAD results bracketed those of Grid 2 and Grid 3, confirming the CFD results with an engineering method. It is also noted that the computed peak convective fluxes are about an order-of-magnitude higher than the computed peak radiative heat fluxes.

Table 1 also shows the computed peak base heat fluxes when the base-to-ground distance is raised 4.3 times. Both the computed convective and radiative heat fluxes dropped significantly from those of testing on pad. This is a result of the fountain jet attaching to two of the nozzle plumes due to the Coanda effect.

SUMMARY AND CONCLUSIONS

This study provided base heating environments for the testing of a four-engine lunar lander demonstrator on pad and hovering at a distance over ground, using an anchored computational methodology. Important near-ground base flow physics captured include the fountain jet, plume afterburning, nozzle plume-to-ground impingement, fountain jet-to-base impingement, base wall jet, and exhaust plume growth. More importantly, due to the specific geometry and operating conditions, it is found that the Coanda effect prominently affected the fountain jet behaviors. When testing the lunar lander demonstrator on pad, the Coanda effect precursor makes the fountain jet oscillate about the central dome base, but the fountain jet itself never attaches to any of the plumes. Conversely, when the lunar lander demonstrator is hovering over ground, the Coanda effect forces the fountain jet to be attached to two of the nozzle plumes, significantly reducing the base heat fluxes.

ACKNOWLEDGMENTS

REFERENCES

[1] FDNS – A General Purpose CFD code, User's Guide, Engineering Sciences, Inc., Huntsville, Alabama, ESI-TR-97-01, May 1997.

[2] Wang, T.-S., "Delta Clipper-Experimental In-Ground Effect on Base Heating Environment," Journal of Thermophysics and Heat Transfer, Vol. 12, No. 3, July-Sept., 1998, pp. 343-349. doi: 10.2514/2.6367

[3] Mehta, M., Gaddy, D.E., Danehy, P. M., Inman, J. A., Parker, R., and Dufrene, A. T., "Optical Diagnostic Imaging of Multi-Rocket Plume-Induced Base Flow Environments," AIAA Paper 2017-3465, June 2017.

[4] UNIC-UNS User's Manual – A General Purpose CFD Code Using Unstructured Mesh, Engineering Sciences, Inc., Huntsville, Alabama, 2006.

[5] Chen, Y. S., Lai, A., Lin, J. W., Wei, S. S., Chou, T. H., and Wu, J. S., "Investigation on Tri-Propellant Hybrid Rocket Performance," AIAA Paper 2016-4659, July 2016.

[6] Wang, T.-S., "Multidimensional Unstructured-Grid Liquid Rocket Engine Nozzle Performance and Heat Transfer Analysis," *Journal of Propulsion and Power,* Vol. 22, No. 1, January-February, 2006, pp. 78-84.

[7] Shang, H. M., and Chen, Y. S., "Unstructured Adaptive Grid method for Reacting Flow Computation," AIAA Paper 1997-3183, July 1997.

[8] Chang, G., Ito, Y., Ross, D., Chen. Y.-S., Zhang S., and Wang, T.-S., "Numerical Simulations of Single Flow Element in a Nuclear Thermal Thrust Chamber" AIAA Paper 2007-4143, June 2007.

[9] Wang, T.-S., Chen, Y.-S., Liu, J., Myrabo, L.N., and Mead, F.B. Jr., "Advanced Performance Modeling of Experimental Laser Lightcraft," *Journal of Propulsion and Power,* Vol. 18, No. 6, 2002, pp. 1129-1138.

[10] Zhang, S. J., Liu, J. W., Chen, Y. S., Godavarty, D., Mallaoragada, P., and Wang, T. S., "A Parallelized Adaptive, Multi-Grid Hybrid Unstructured Solver for All-Speed Flows," AIAA Paper, 2002-0109, January 2002.

[11] Wang, T.-S., Droege, A., D'Agostino, M., Lee, Y.-C., and Williams, R., "Asymmetric Base-Bleed Effect on X-33 Aerospike Plume Induced Base-Heating Environment," *Journal of Propulsion and Power,* Vol. 20, No. 3, 2004, pp. 385-393.

[12] Chen, Y.-S., and Kim, S. W., "Computation of Turbulent Flows Using an Extended k-ε Turbulence Closure Model," NASA CR-179204, Oct. 1987.

[13] Liu, J. W., Chen, Y. S., "Parallel Simulation of Radiative Heat Transfer using an Unstructured Finite-Volume Method," *Numerical Heat Transfer*, Part B, Vol. 36, pp. 115-137, 1999.

[14] Liu, J. W., Chen, Y. S., "Development of an Unstructured Radiation Model Applicable for Two-dimensional Planar, Axisymmetric and Three-dimensional Geometries," *J. of Quantitative Spectroscopy & Radiative Transfer*, Vol. 22, pp. 17-33, 2000.

[15] Liu, J., Shang, H. M., Chen, Y. S., and Wang, T. S., "GRASP: A General Radiation Simulation Program," AIAA Paper 97-2559, June 1997.

[16] Wang, T.-S., "Grid-Resolved Analysis of Base Flowfield for Four-Engine Clustered Nozzle Configuration," Journal of Spacecraft and Rockets, Vol. 33, No. 1, January-February 1996, pp.22-29. doi: 10.2514/3.55702

[17] Wang, T.-S., and Cornelison, J. "Analysis of Flowfields over Four-Engine DC-X Rockets," *Journal of Spacecraft and Rockets*, Vol. 34, No. 5, Sept.-Oct., 1997, pp. 620-627.

[18] Wang, T.-S., "Analysis of Linear Aerospike Plume Induced X-33 Base-Heating Environment," Journal of Spacecraft and Rockets, Vol. 36, No. 6, Nov.–Dec., 1999, pp. 777-783.

[19] Wang, T.-S., "Effect of Fence on Linear Aerospike Plume Induced Base-Heating Physics," Journal of Thermophysics and Heat Transfer, Vol. 14, No. 4, October-December, 2000, pp. 457-463.

[20] Smith, S. D., "Unified Test Stand Design and Environmental Impact Model," PT-FR-03-01, Plumtech, Huntsville, AL. July 2003.

[21] Reardon, J. E., and Lee, Y. C., "A Computer Program for Thermal Radiation from Gaseous Rocket Plumes (GASRAD)," Remtech RTR 014-09, December 1979.

[22] Ludwig, C., et al., "Handbook of Infrared Radiation from Combustion Gases," NASA SP 3080, 1973.

[23] Tritton, D. J., Physical Fluid Dynamics. Van Nostrand Reinfold, 1977 (reprinted 1980), Section 22.7, The Coanda Effect.